THE JOURNAL OF PHYSICAL CHEMISTRY LETTERS
A JOURNAL OF THE AMERICAN CHEMICAL SOCIETY

pubs.acs.org/JPCL

Letter

Exploring Chalcohalide Perovskite-Inspired Materials ($Sn_2SbX_2I_3$; X = S or Se) for Optoelectronic and Spintronic Applications

Manish Kumar,* Sajjan Sheoran, and Saswata Bhattacharya*

Cite This: *J. Phys. Chem. Lett.* 2023, 14, 10158−10165

Read Online

ACCESS | Metrics & More | Article Recommendations | Supporting Information

ABSTRACT: Chalcohalide perovskite-inspired materials have attracted attention as promising optoelectronic materials due to their small band gaps, high defect tolerance, nontoxicity, and stability. However, a detailed analysis of their electronic structure and excited-state properties is lacking. Here, using state-of-the-art density functional theory, an effective **k·p** model analysis, and many-body perturbation theory (within the framework of *GW* and BSE), we explore the band splitting and excitonic properties of $Sn_2SbX_2I_3$ (X = S or Se). Our findings reveal that the $Cmc2_1$ phase exhibits Rashba and Dresselhaus effects, causing significant band splitting, especially near the conduction and valence band extremes, respectively. Moreover, we find that the exciton binding energy is larger than those of lead halide perovskites but smaller than those of chalcogenide perovskites. We also investigate polaron-facilitated charge carrier mobility, which is found to be similar to that of lead halide perovskites and greater than that of chalcogenide perovskites. These characteristics make these materials promising for applications in spintronics and optoelectronics.

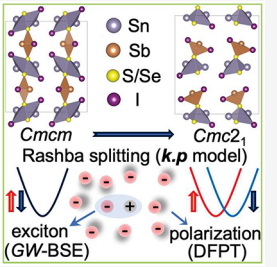

Perovskites (ABX_3 compounds, where A and B are cations and X is an anion) make up a versatile family of materials exhibiting a vast range of properties, including the photovoltaic effect, the photocatalytic effect, ferroelectricity, piezoelectricity, and superconductivity.[1] In recent years, lead-based inorganic−organic hybrid halide perovskite solar cells have shown an unprecedented increase in power conversion efficiency from 3.8% to 25.7%.[2,3] This is attributed to their exceptional properties for a solar cell absorber, such as a high absorption coefficient of $\sim 10^5$ cm^{-1} in the visible wavelength range, small exciton binding energies of ∼20 meV, long charge carrier diffusion lengths of $\lesssim$100 μm, excellent charge carrier mobilities, a tunable band gap, and high defect tolerance.[4,5] Moreover, these can be fabricated via simple solution deposition, resulting in low-cost manufacturing. However, their commercialization is impeded by several factors. (i) The efficiency decreases with an increase in the size of the thin films of lead halide perovskites (LHPs). (ii) The material becomes unstable upon exposure to humidity, heat, or light. (iii) Poisonous lead can harm the environment and living organisms.[6] The thermal stability of hybrid LHPs could be improved by the utilization of an inorganic cation at the A site instead of an organic one, but all inorganic LHPs still suffer from long-term instability under operational conditions, especially against moisture stress.[7] These challenges, alongside the high performance of LHPs, stimulate the research in lead-free and stable perovskite-inspired materials (PIMs).[8]

The presence of ns^2 lone-pair electrons on the Pb cation can be crucial in fostering exceptional optoelectronic performance in LHPs.[9] In combination with a halide anion, this lone-pair cation leads to small effective masses for electrons and holes, defect tolerance, and strong dielectric screening.[10,11] A wide range of compounds comprising Pb^{2+}, Sn^{2+}, Ge^{2+}, Sb^{3+}, and Bi^{3+} cations containing ns^2 electronic configurations are currently of interest as light harvesters.[12] Among them, chalcohalide PIMs have emerged as promising materials having an ns^2 electronic configuration as well as a cation−halide combination.[11,13,14] Recently, Nie et al.[13] have synthesized a solar cell based on tin−antimony sulfoiodide ($Sn_2SbS_2I_3$) using a single-step, solution-based chemical deposition process, exhibiting a power conversion efficiency (PCE) of 4.04%. They have also demonstrated its stability against air, moisture, and light illumination. The achievement of a PCE surpassing the initially reported value for methylammonium lead iodide[2] has significant potential. $Sn_2SbS_2I_3$ has long been known,[15,16] but the recent surge of interest in it stems from its considerable potential in various optoelectronic applications.[13,17,18] In view of this, we aim to provide an in-depth theoretical study of chalcohalide PIMs ($Sn_2SbX_2I_3$; X = S or Se) to investigate the atomistic origins of their appealing optoelectronic properties that may act as valuable guidance for further development of this emerging material class.

Note that the presence of heavy elements in PIMs, such as Sb and I, imparts a strong spin−orbit coupling (SOC), playing a significant role in determining the electronic properties. When the SOC is combined with the crystal's broken inversion

Received: September 4, 2023
Revised: October 27, 2023
Accepted: October 31, 2023
Published: November 5, 2023

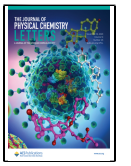

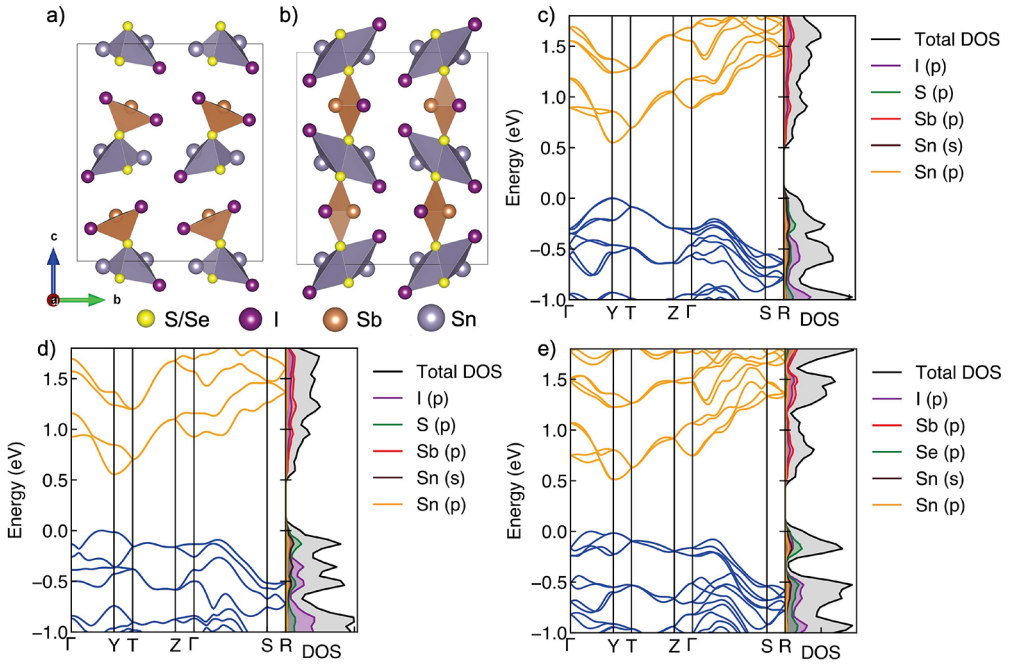

Figure 1. Schematic crystal structure of orthorhombic $Sn_2SbX_2I_3$ (X = S or Se) in the (a) $Cmc2_1$ and (b) $Cmcm$ phases. Electronic band structure and partial density of states (pDOS) of (c) $Sn_2SbS_2I_3$ in the $Cmc2_1$ phase, (d) $Sn_2SbS_2I_3$ in the $Cmcm$ phase, and (e) $Sn_2SbSe_2I_3$ in the $Cmc2_1$ phase using PBE+SOC.

symmetry, it results in Rashba band splitting. The Rashba effect is considered to be a possible cause of the reduced recombination rate and longer carrier lifetimes in LHPs.[19,20] Nonetheless, it has been demonstrated[21] that employing a Rashba Hamiltonian within a tight-binding model[19] can result in an inaccurate depiction of spin orientations at the band extrema. Therefore, the Rashba effect must be carefully determined to find the right implications. In the case of organic−inorganic LHPs, the mismatch of crystal momentum between the valence band maximum (VBM) and conduction band minimum (CBM) due to the Rashba effect may be the cause of the reduction in the recombination rate.[22] Moreover, the Rashba effect opens up the possibility of these materials being used in spintronics. We, therefore, attempt to study the Rashba effect in chalcohalide PIMs, which generally enhances the efficiency of optoelectronic devices and potentially expedites their usage in spintronic devices.

An important aspect of solar cell application is charge separation, which depends on the formation of excitons. The dissociation of excitons into free electrons and holes brings about the desired free charge transport. Therefore, accurate determination of excited-state properties, such as exciton binding energy, is necessary to understand and possibly improve the photovoltaic performance. In addition, the role of electron−phonon interaction is crucial in assimilating the excitation dynamics.[23] This could be understood in terms of polaron formation, which can influence charge carrier mobility. To this end, presumably for the first time, we have systematically investigated the excitonic and polaronic properties of chalcohalide PIMs by advanced theoretical methodologies.

In this Letter, we analyze the Rashba and Dresselhaus effects in chalcohalide PIMs ($Sn_2SbX_2I_3$; X = S or Se) using density functional theory (DFT)[24,25] calculations and a symmetry-adapted **k·p** model Hamiltonian. In addition, their optical properties are characterized using many-body perturbation theory (MBPT) in the framework of the G_0W_0[26,27] approximation and the Bethe−Salpeter equation (BSE).[28,29] The static dielectric constants are calculated using density functional perturbation theory (DFPT). Finally, using the Fröhlich model,[30,31] we determine the polaronic properties.

Recently, Kavanagh et al.[11] have reported that the $Cmc2_1$ phase of $Sn_2SbS_2I_3$ is more stable than the $Cmcm$ phase and the experimental $Cmcm$ phase is the result of macroscopic averaging over local $Cmc2_1$ configurations. This kind of polymorphism is also found in LHPs and goes undetected by X-ray diffraction (XRD) due to the long coherence length.[32,33] Its impact is evident in determining the thermodynamic stability and optoelectronic properties. Therefore, in this work, we consider both phases ($Cmc2_1$ and $Cmcm$) of $Sn_2SbS_2I_3$ and the $Cmc2_1$ phase of $Sn_2SbSe_2I_3$ (see Figure 1a,b). The initial orthorhombic geometries of $Sn_2SbX_2I_3$ (X = S or Se) were obtained from the Materials Project repository.[34] The lattice parameters of the optimized structures calculated using the optB86b-vdW[35] exchange-correlation (ε_{xc}) functional are listed in Table 1. These are in close agreement with previous experimental[15,16,36] and theoretical[11] results. The $Cmcm$ phase consists of $(Sn_2S_2I_2)_n$ chains along the a direction, forming a layered structure in the $a-b$ plane, having I and Sb between the layers (see Figure 1b), whereas in the $Cmc2_1$

Table 1. Calculated Lattice Parameters of $Sn_2SbX_2I_3$ (X = S or Se)[a]

configuration	phase	a (Å)	b (Å)	c (Å)	c/a
$Sn_2SbS_2I_3$	$Cmc2_1$	4.27	14.16	16.40	3.84
	$Cmcm$	4.26	13.93	15.95	3.74
	experiment	4.25	13.99	16.38	3.85
$Sn_2SbSe_2I_3$	$Cmc2_1$	4.32	14.45	17.09	3.96
	experiment	4.30	14.08	17.22	4.00

[a]The experimental values from ref 16 are provided for comparison.

https://doi.org/10.1021/acs.jpclett.3c02475
J. Phys. Chem. Lett. 2023, 14, 10158−10165

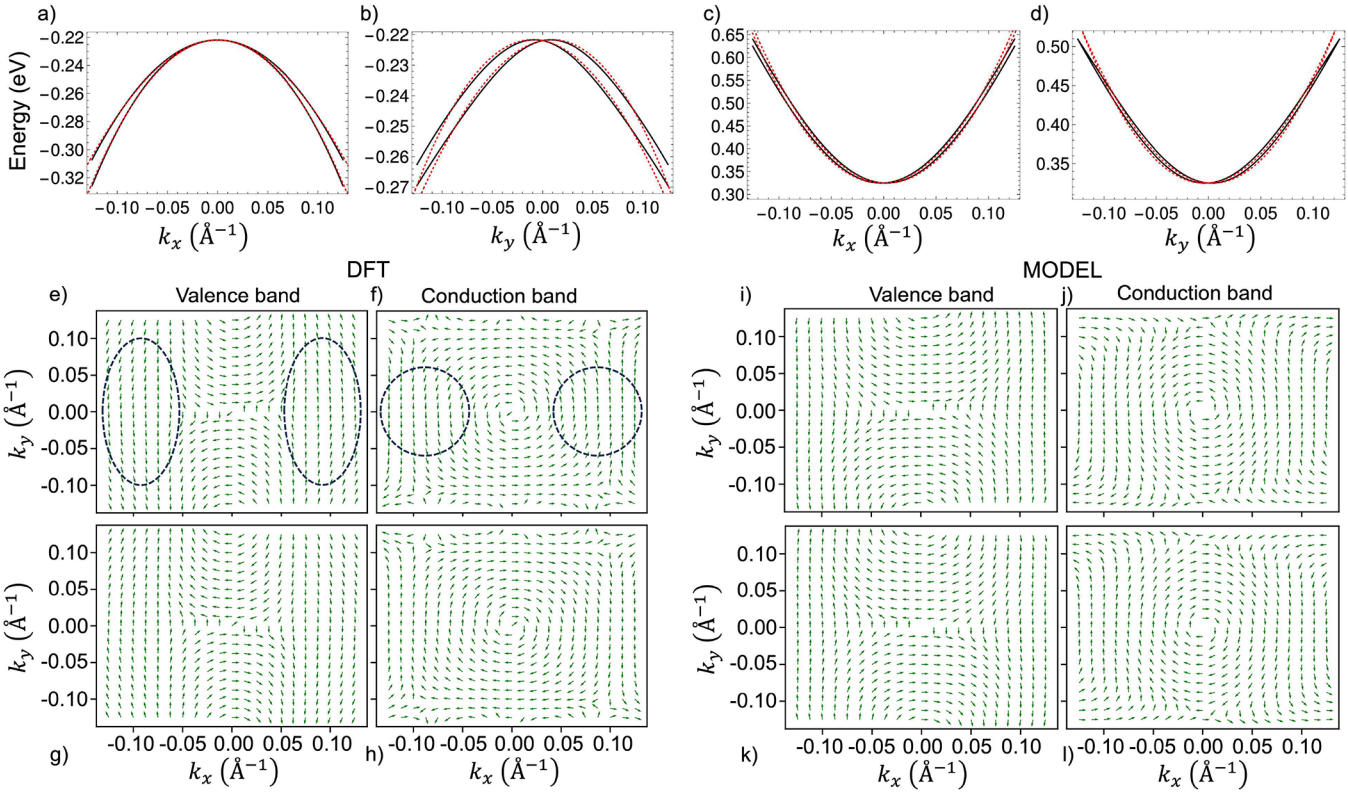

Figure 2. (a and b) Valence bands and (c and d) conduction bands of $Sn_2SbS_2I_3$ along the k_x and k_y directions. The black lines and red dots are bands obtained using the DFT and **k·p** model, respectively. Spin textures of (e and g) the two highest valence bands and (f and h) the two lowest conduction bands, computed using DFT. (i–l) Model-produced spin textures, counterparts of (e–h), respectively. The arrows denote the in-plane spin component. The out-of-plane spin component is zero in the considered range.

phase, there is a small displacement of I, resulting in $(Sn_2SbS_2I_3)_n$ chains along the *a* direction (see Figure 1a). The lattice parameters of both phases are similar along *a* and *b*, with the largest difference being along the *c* direction (see Table 1). More details about bond lengths and bond angles are available in Table S1.

The calculated electronic band structure and partial density of states (pDOS) using the PBE ε_{xc} functional with the inclusion of SOC are shown in Figure 1c–e. From pDOS, we observe that the VBM is dominated by S/Se (p), I (p), and Sn (s) orbitals whereas the CBM is dominated by Sb (p) and I (p) orbitals. The $Cmc2_1$ phase of $Sn_2SbS_2I_3$ has a direct band gap of 0.68 eV at the Y point without including SOC. In the presence of SOC, the band gap is reduced to 0.55 eV. Therefore, the role of SOC is significant in these chalcohalide PIMs and duly considered in all of the calculations. We observe that the bands are spin-degenerate throughout the Brillouin zone in the *Cmcm* phase of $Sn_2SbS_2I_3$ as shown in Figure 1d. This is attributed to the spin degeneracy (Kramer's degeneracy) preserved by the time reversal and inversion symmetry.[37] On the contrary, in the $Cmc2_1$ phase, bands associated with the CBM and VBM split around the Y point due to inversion symmetry breaking (see Figure 1c). To clearly visualize the splitting of bands, we plot the band structure along the k_x and k_y directions around the Y point (see Figure 2a–d). Note that the splitting is absent along the k_z direction due to the presence of mirror ($\bar{M}_x$) and glide ($\bar{M}_y$) planes. The $\bar{M}_x$ and $\bar{M}_y$ planes result in zero polarization along the [100] and [010] planes, respectively. In accordance with the previous reports,[11] we find the electric polarization along *z* with a magnitude of 36 μC/cm^2. The spin splitting occurs only in the plane perpendicular to the polarization direction (k_x–k_y plane in our case). Furthermore, we have plotted the spin textures of the CBM and VBM around the Y point (see Figure 2e–h). The in-plane spin textures are chiral, with opposite orientations for the inner and outer bands, while the out-of-plane spin texture is zero. The spin texture and splitting around the Y point can be understood in terms of the **k·p** Hamiltonian derived using the symmetry considerations.[38−40] The group of wave vectors associated with the Y point includes symmetry operations $\{2_{100}|00\frac{1}{2}\}(\bar{C}_{2z})$, $\{m_{100}|000\}(\bar{M}_x)$, and $\{m_{010}|00\frac{1}{2}\}(\bar{M}_y)$ (see the Bilbao Crystallographic Server[41] for notation). Note that the transformation rules of **k** under the glide plane and screw axis are the same as that of the associated mirror and rotation operations, respectively.[42] The transformation rules of (k_x, k_y, k_z) and Pauli matrices $(\sigma_x, \sigma_y, \sigma_z)$ denoting the spin degrees of freedom under $\bar{C}_{2z}$, $\bar{M}_x$, and $\bar{M}_y$ are listed in Table 2.

Table 2. Transformation Rules of (k_x, k_y, k_z) and $(\sigma_x, \sigma_y, \sigma_z)$ under the Symmetry Operation Belonging to the Group of the Wave Vector of the Y Point and Time Reversal Operation (T)[a]

operation	(k_x, k_y, k_z)	$(\sigma_x, \sigma_y, \sigma_z)$	invariants
$\bar{C}_{2z}$	$(-k_x, -k_y, k_z)$	$(-\sigma_x, -\sigma_y, \sigma_z)$	$k_i\sigma_j$ $(i, j = x, y)$, $k_z\sigma_z$
$\bar{M}_x$	$(-k_x, k_y, k_z)$	$(\sigma_x, -\sigma_y, -\sigma_z)$	$k_x\sigma_y$, $k_y\sigma_x$, $k_z\sigma_x$
$\bar{M}_y$	$(k_x, -k_y, k_z)$	$(-\sigma_x, \sigma_y, -\sigma_z)$	$k_x\sigma_y$, $k_y\sigma_x$, $k_z\sigma_y$,
T	$(-k_x, -k_y, -k_z)$	$(-\sigma_x, -\sigma_y, -\sigma_z)$	$k_i\sigma_j$ $(i, j = x, y, z)$

[a]Wave vector **k** is referenced from the Y point.

https://doi.org/10.1021/acs.jpclett.3c02475
J. Phys. Chem. Lett. 2023, 14, 10158−10165

Table 3. Parametrization of $\alpha_{(1)}$, $\alpha_{(3)}$, $\beta_{(1)}$, $\beta_{(3)}$, γ_α, and γ_β for the Lowest Conduction Bands and Top Valence Bands (around the Y point) of $Sn_2SbX_2I_3$ (X = S or Se) Having $Cmc2_1$ Group Symmetry[a]

	band	$\alpha_{(1)}$ (eV Å)	$\alpha_{(3)}$ (eV Å^3)	γ_α (eV Å^3)	$\beta_{(1)}$ (eV Å)	$\beta_{(3)}$ (eV Å^3)	γ_β (eV Å^3)
$Sn_2SbS_2I_3$	VB	0.005	3.796	1.013	0.065	−3.595	0.508
	CB	0.115	−4.877	0.883	−0.094	5.838	1.002
$Sn_2SbSe_2I_3$	VB	0.007	5.211	2.132	0.081	−6.592	1.213
	CB	0.131	−5.126	0.658	−0.099	4.892	0.995

[a]The k_x and k_y ranges considered to fit our models are within 0.125 Å^{-1}.

The **k·p** Hamiltonian characterizing the spin splitting in the k_z = 0 plane is obtained by collecting all of the symmetry invariant terms up to cubic in **k** and expressed as

$$H = H_0 + \alpha(\mathbf{k})k_x\sigma_y + \beta(\mathbf{k})k_y\sigma_x \quad (1)$$

where H_0 is the free particle Hamiltonian. $\alpha(\mathbf{k})$ and $\beta(\mathbf{k})$ are the splitting coefficients determining the strength of SOC, given by

$$\alpha(\mathbf{k}) = \alpha_{(1)} + \alpha_{(3)}(k_x^2 + k_y^2) + \gamma_\alpha(k_x^2 - k_y^2)$$
$$\beta(\mathbf{k}) = \beta_{(1)} + \beta_{(3)}(k_x^2 + k_y^2) + \gamma_\beta(k_x^2 - k_y^2) \quad (2)$$

where $\alpha_{(3)}$ and $\beta_{(3)}$ terms take cubic interaction into consideration and γ_α and γ_β take the cubic anisotropy into consideration. Note that σ_z terms with a linear dependence in **k** are forbidden by symmetry, resulting in the vanishing out-of-plane spin component. We have fitted the band structure around the Y point and parametrized α and β. The results are shown in Figure 2a−d, and the corresponding splitting parameters are listed in Table 3. As one can clearly see in Figure 2a, valence bands are almost cubic split along the k_x direction, signifying the crucial role of the $\alpha_{(3)}$ and $\gamma_{(\alpha)}$ terms in the Hamiltonian. The cubically split bands provide an additional advantage over linear splitting in spintronics, i.e., the larger spin Hall conductivity and spin transport in a system with higher spin (spin 1 and spin $^3/_2$ quasiparticles).[43−45] In the regime of purely linear splitting, the strength of linear Rashba and Dresselhaus effects is obtained using

$$\alpha_R = \frac{\alpha_{(1)} - \beta_{(1)}}{2}$$
$$\alpha_D = \frac{\alpha_{(1)} + \beta_{(1)}}{2} \quad (3)$$

where α_R and α_D are Rashba and Dresselhaus parameters, respectively. For the VB, we find α_R = 0.030 eV Å and α_D = 0.035 eV Å. Similarly, for the CB of $Sn_2SbS_2I_3$, α_R = 0.105 eV Å and α_D = 0.010 eV Å. Therefore, the linear Rashba effect dominates the Dresselhaus effect for the CB splitting. This is also evident from the helical spin textures shown in Figure 2f. On the contrary, in the case of spin splitting of the VB, the contribution of both linear Rashba and Dresselhaus is significant, with linear Dresselhaus being the dominant one. The larger CB splitting is attributed to the heavier Sb (p) orbitals' contribution to the CB in comparison to the S (p) and Sn (s) orbitals' contribution to the VB (see Figure 1c). Furthermore, we have also plotted the spin textures of CB and VB using the **k·p** Hamiltonian with the parameters listed in Table 3. The **k·p** model-produced spin textures are in good agreement with the DFT spin textures (see Figure 2e−l). Similar spin splittings and textures are also observed in the $Cmc2_1$ phase of $Sn_2SbSe_2I_3$ (see Table 3 for parameters). However, the strength of the splitting is slightly larger in the case of $Sn_2SbSe_2I_3$ owing to larger SOC coming from the Se atom than from the S atom. We also note that **k·p** model spin textures may deviate from the DFT spin textures far from the Y point because the model is applicable only in the immediate proximity of the Y point. Interestingly, spin textures for CB and VB are nearly **k**-independent near $k_x = \pm 0.1$ Å^{-1} (see dashed regions in Figure 2e,f). Such quasi-persistent spin textures promise nondephasing spin transport through a persistent spin helix mechanism.[46,47] Additionally, these spin textures can be reversed through polarization switching with an energy barrier of 35 meV/atom.

From the band structures, we observe the large dispersion at the CBM and VBM, with the former being more dispersive (see Figure 1c−e). Therefore, charge carrier transport would be better in these chalcohalide PIMs. The effective masses along different high-symmetry paths due to their anisotropic nature are listed in Table 4. The $Cmc2_1$ phase of $Sn_2SbS_2I_3$ has a direct band gap at the Y point, whereas the band gap is indirect in the case of the *Cmcm* phase of $Sn_2SbS_2I_3$ and $Sn_2SbSe_2I_3$. The VBM is shifted, lying between Y and Γ in the latter cases. Note that the semilocal ε_{xc} functional PBE underestimates the band gap due to the well-known self-interaction error. The band gaps are corrected by using MBPT in the framework of single-shot *GW* (G_0W_0) calculations. The band profile remains similar to PBE+SOC, but the band gap opens up (see Figure S1 for the band structure obtained using G_0W_0). The band gaps are improved in comparison to previously reported theoretical[11] values calculated using HSE06+SOC but underestimated by ∼0.3 eV with respect to experimentally reported values[13,36] (see Table 5).

Table 4. Effective Masses of the Electron and Hole (in terms of free-electron mass m_e) of Chalcohalide PIMs along the High-Symmetry Path

configuration	phase	m_e^*	m_h^*
$Sn_2SbS_2I_3$	$Cmc2_1$	0.26 (Y-Γ)	0.95 (VBM-Γ)
		0.90 (Y-T)	
	Cmcm	0.33 (Y-Γ)	1.40 (VBM-Γ)
		0.86 (Y-T)	1.32 (VBM-Y)
$Sn_2SbSe_2I_3$	$Cmc2_1$	0.27 (Y-Γ)	0.71 (VBM-Γ)
		1.13 (Y-T)	1.49 (VBM-Y)

Table 5. Band Gaps (in electronvolts) of Chalcohalide PIMs

configuration	phase	PBE +SOC	G_0W_0@PBE +SOC	previously reported
$Sn_2SbS_2I_3$	$Cmc2_1$	0.55	1.20	1.08[11]
	Cmcm	0.56	1.10	1.02,[11] 1.41[13]
$Sn_2SbSe_2I_3$	$Cmc2_1$	0.51	1.11	

https://doi.org/10.1021/acs.jpclett.3c02475
J. Phys. Chem. Lett. 2023, 14, 10158−10165

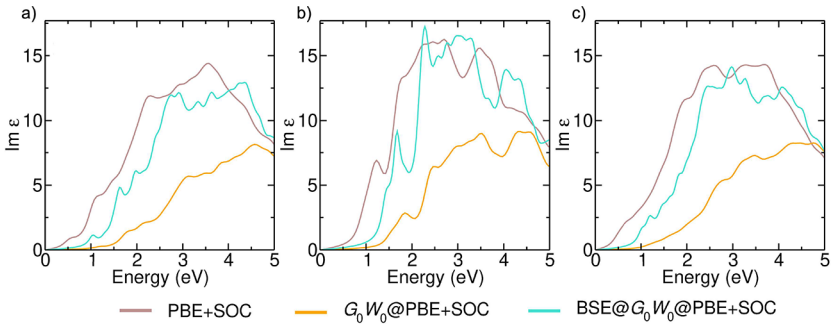

Figure 3. Spatially averaged imaginary part [Im ε] of the dielectric function for (a) $Sn_2SbS_2I_3$ in the $Cmc2_1$ phase, (b) $Sn_2SbS_2I_3$ in the $Cmcm$ phase, and (c) $Sn_2SbSe_2I_3$ in the $Cmc2_1$ phase, obtained using PBE+SOC, G_0W_0@PBE+SOC, and BSE@G_0W_0@PBE+SOC.

Table 6. Polaron Mobilities of Chalcohalide PIMs at Room Temperature (T = 300 K)[a]

configuration	phase	Ω (THz)	ε_S	ε_∞	α	r_F (10^{-9} m)	m_p	μ_H (cm^2 V^{-1} s^{-1})
$Sn_2SbS_2I_3$	$Cmc2_1$	4.20	22.95	10.78	0.70	7.94	0.29	202.93
	$Cmcm$	1.42	93.22	13.09	1.82	2.18	0.40	90.16
$Sn_2SbSe_2I_3$	$Cmc2_1$	2.76	22.66	11.64	0.74	5.60	0.30	214.94

[a] ε_S and ε_∞ are given in units of the permittivity of free space (ε_0). Effective polaron mass m_p is given in units of free electron mass (m_e).

The dielectric function is obtained by solving BSE on top of G_0W_0@PBE+SOC. The imaginary part of the dielectric function [Im ε] is shown in Figure 3. As per the BSE eigenvalue analysis, the energy positions corresponding to the first bright exciton (optically active) lie at 1.02, 1.28, and 1.01 eV for the $Cmc2_1$ and $Cmcm$ phases of $Sn_2SbS_2I_3$ and the $Cmc2_1$ phase of $Sn_2SbSe_2I_3$, respectively. A dark exciton also exists at nearly the same energy position as a bright exciton in the $Cmc2_1$ phase of $Sn_2SbX_2I_3$ (X = S or Se). On the contrary, many dark excitons exist below bright excitons in the $Cmcm$ phase of $Sn_2SbS_2I_3$. This can be seen from the oscillator strength given in Table S2. Moreover, the main shoulder peak lies at ∼1.4 eV (see Figure 3b), which agrees with the experimental band gap of 1.4 eV measured by Nie et al.[13] and 1.5 eV obtained by Starosta et al.[36] The dielectric functions are anisotropic, and the contributions of different components are shown in Figure S2. Note that the exciton binding energy (E_B) can be determined by taking the difference of the peak positions obtained from G_0W_0 and BSE. Hence, the E_B values of the optically active exciton for the $Cmc2_1$ and $Cmcm$ phases of $Sn_2SbS_2I_3$ and the $Cmc2_1$ phase of $Sn_2SbSe_2I_3$ are found to be ∼173, ∼136, and ∼103 meV, respectively. These exciton binding energies are larger in comparison for the LHPs[48] but smaller than for the chalcogenide perovskites.[49] Using the dielectric function, we find the absorption coefficient to be on the order of ∼10^5 cm^{-1} in the visible-light region (see Figure S3), which is promising from the perspective of application in optoelectronic devices.

In addition, to gain a deeper understanding of the fundamental limits of mobility, it would be beneficial to make a first-principles prediction.[31,50] While theories of mobility are being developed, it is important to take into account the polaron state, which results from strong interactions between charge carriers and phonons rather than solely considering the free carrier state. Fröhlich developed a Hamiltonian that describes the interaction between independent electrons (i.e., those with a low density) and polar optical phonons. The dimensionless Fröhlich parameter α of dielectric electron−phonon coupling is

$$\alpha = \frac{1}{4\pi\varepsilon_0}\frac{1}{2}\left(\frac{1}{\varepsilon_\infty} - \frac{1}{\varepsilon_S}\right)\frac{e^2}{\hbar\Omega}\left(\frac{2m^*\Omega}{\hbar}\right)^{1/2} \quad (4)$$

The characteristics of the optical (ε_∞) and static (ε_S) dielectric constants, the effective mass (m^*) of the bare-electron band, and a characteristic phonon angular frequency (Ω) completely determine it. The values of the Planck constant ($\hbar$), the permittivity of free space (ε_0), and the electron charge (e) are also relevant. We find that the polaron in these materials lies in the intermediate regime (α = 0.70−1.82) (see Table 6).

Feynman devised a novel approach to solving the Fröhlich Hamiltonian, where the electron interacts with a group of independent phonon excitations that behave harmonically and are integrated over the quantum field.[51] The electron interacts with the perturbation it causes when passing through the lattice, and it decays exponentially over time. In Feynman's method, the effective mass of the polaron (for a small α) is expressed as follows

$$m_p = m^*\left(1 + \frac{\alpha}{6} + \frac{\alpha^2}{40} + ...\right) \quad (5)$$

This expression shows that the polaron mass is always higher than the effective mass of Bloch's electron. We observe that electron−phonon coupling causes the polaron mass to be increased by ∼11−20% (see Tables 4 and 6). We have used the finite temperature model devised by Osaka[52] to describe the polaron based on the path integral calculations demonstrated by Feynman.[51] In this model, the self-free energy of the polaron (F) is calculated using two free parameters, v and w. We numerically find v and w that minimize $F = -(A + B + C)$,[53] where

$$A = \frac{3}{\beta}\left[\ln\left(\frac{v}{w}\right) - \frac{\ln(2\pi\beta)}{2} - \ln\frac{\sinh\left(\frac{v\beta}{2}\right)}{\sinh\left(\frac{w\beta}{2}\right)}\right] \quad (6)$$

https://doi.org/10.1021/acs.jpclett.3c02475
J. Phys. Chem. Lett. 2023, 14, 10158−10165

$$B = \frac{\alpha v}{\sqrt{\pi}[\exp(\beta) - 1]} \int_0^{\beta/2} \frac{\exp(\beta - x) + \exp(x)}{\sqrt{w^2 x\left(1 - \frac{x}{\beta}\right) + \frac{Y(x)(v^2 - w^2)}{v}}} \, dx \quad (7)$$

$$Y(x) = \frac{1}{1 - \exp(-v\beta)}\{1 + \exp(-v\beta) - \exp(-vx) - \exp[v(x - \beta)]\} \quad (8)$$

$$C = \frac{3(v^2 - w^2)}{4v}\left[\coth\left(\frac{v\beta}{2}\right) - \frac{2}{v\beta}\right] \quad (9)$$

where $\beta = \hbar\Omega/k_B T$ is the phonon occupation factor and v is the frequency of relative motion between longitudinal optical (LO) phonon and charge carrier. The expected value of the squared distance between phonon and charge carrier defines the polaron size (r_F)[53]

$$r_F = \sqrt{\frac{3\hbar v}{2m^*(v^2 - w^2) \times 2\pi\Omega}} \quad (10)$$

In the theory, Hellwarth et al.[54] defined the polaron mobility by contour integrating the self-energy of the perturbed polaron[53,55,56]

$$\mu_H = \frac{3\sqrt{\pi}e}{\Omega m * \alpha} \frac{\sinh(\beta/2)}{\beta^{5/2}} \frac{w^3}{v^3} \frac{1}{K} \quad (11)$$

$$K = \int_0^\infty \frac{\cos(u)}{[u^2 + a^2 - b\cos(vu)]^{3/2}} \, du \quad (12)$$

$$a^2 = \left(\frac{\beta}{2}\right)^2 + \left(\frac{v^2 - w^2}{w^2 v}\right)\beta \coth\left(\frac{\beta v}{2}\right) \quad (13)$$

$$b = \left(\frac{v^2 - w^2}{w^2 v}\right)\frac{\beta}{\sinh\left(\frac{\beta v}{2}\right)} \quad (14)$$

At 300 K, we predict Hellwarth polaron mobilities of 202.93 and 90.16 $cm^2\ V^{-1}\ s^{-1}$ in the $Cmc2_1$ and $Cmcm$ phases of $Sn_2SbS_2I_3$, respectively. The $Cmc2_1$ phase has higher polaron mobility compared to that of the $Cmcm$ phase due to a small static dielectric constant and a higher phonon angular frequency. Similarly, the calculated polaron mobility is 214.94 $cm^2\ V^{-1}\ s^{-1}$ in the $Cmc2_1$ phase of $Sn_2SbSe_2I_3$. The calculated parameters for the polarons, i.e., Fröhlich parameter (α), polaron size (r_F), LO phonon characteristic frequency (Ω), polaron mass (m_p), and polaron mobility (μ_H), are listed in Table 6. We notice that the polaron mobility of these chalcohalide PIMs is comparable to that of LHPs[31] and larger than that of chalcogenide perovskites.[49,57]

In conclusion, we have investigated the band splitting and excited-state properties of chalcohalide perovskite-inspired materials (PIMs) ($Sn_2SbX_2I_3$; X = S or Se) by state-of-the-art density functional theory, an effective **k·p** model, and many-body perturbation theory. We observed that spin−orbit coupling (SOC) significantly affects the electronic structure in these chalcohalide PIMs. The calculated effective masses of electrons are found to be small, suggesting good charge carrier mobility. The $Cmc2_1$ phase of $Sn_2SbX_2I_3$ (X = S or Se) shows Rasbha and Dresselhaus effects, with the former being more dominant for conduction band splitting. The band gaps are corrected by the many-body perturbation theory approach, namely G_0W_0. The exciton binding energies are found to be 173, 136, and 103 meV for the $Cmc2_1$ phase of $Sn_2SbS_2I_3$, the $Cmcm$ phase of $Sn_2SbS_2I_3$, and the $Cmc2_1$ phase of $Sn_2SbSe_2I_3$, respectively. The electron−phonon coupling strength is small in these chalcohalide PIMs, resulting in an intermediate polaron. The $Cmc2_1$ phase of $Sn_2SbS_2I_3$ has a larger polaron mobility in comparison to that of the $Cmcm$ phase. Overall, these results are expected to expedite the research and use of chalcohalide PIMs in optoelectronic and spintronic devices.

COMPUTATIONAL METHODS

The DFT calculations were performed using the Vienna *ab initio* simulation package (VASP).[58,59] The projector-augmented wave (PAW) pseudopotentials[59,60] were used to describe the interactions between electrons and ions for all of the species. The PAW pseudopotentials with valence-electron configurations $4d^{10}5s^25p^2$, $4d^{10}5s^25p^3$, $3s^23p^4$, $4s^24p^4$, and $5s^25p^5$ were considered for Sn, Sb, S, Se, and I, respectively. All of the structures were optimized using the optB86b-vdW ε_{xc} functional until the forces were smaller than 0.001 eV/Å. The functional validation for geometry optimization is given in Table S3. The calculations were performed with a 16-atom primitive unit cell. The tolerance for electronic self-consistent iteration was kept at 1×10^{-6} eV, and a plane-wave kinetic energy cutoff of 350 eV was used with the standard PAW radial cutoffs. A k-point mesh of $4 \times 4 \times 2$ was used for Brillouin zone integration, generated using the Γ-centered Monkhorst−Pack[61] scheme. The effective masses were calculated from the band structures obtained by the PBE ε_{xc} functional. The band structures were generated using SUMO,[62] and the parabolic fitting of the band edges was considered for effective mass calculations. Note that the van der Waals interactions (two-body TkatchenkoScheffler[63]) and spin−orbit coupling (SOC) were also considered. The quasiparticle band gaps were obtained from single-shot GW[26,27] (G_0W_0) calculations. To determine the excited-state properties, the Bethe−Salpeter equation (BSE)[28,29] was solved on top of G_0W_0 calculations. The PBE+SOC was considered as a starting point for G_0W_0 calculations. For polarizability calculations, a grid of 60 frequency points was used. A sufficiently large number of unoccupied bands was considered (for the convergence of empty states, see Table S4). A Γ-centered $4 \times 4 \times 1$ k-point mesh was used for BSE calculations. The electron−hole kernel for BSE calculations was constructed using 64 occupied and 64 unoccupied states (see Figure S4 for convergence). The density functional perturbation theory (DFPT) calculations were carried out with a k-point mesh of $12 \times 12 \times 3$, generated using the Γ-centered Monkhorst−Pack scheme. The polaron mobility was calculated using the code PolaronMobility.jl.

ASSOCIATED CONTENT

Supporting Information

The Supporting Information is available free of charge at https://pubs.acs.org/doi/10.1021/acs.jpclett.3c02475.

Structural characterization of $Sn_2SbX_2I_3$ (X = S or Se), optical transitions calculated using BSE, effect of different functionals on the lattice parameters of $Sn_2SbS_2I_3$, convergence of a number of bands used in G_0W_0 calculations, band structure obtained using G_0W_0

https://doi.org/10.1021/acs.jpclett.3c02475
J. Phys. Chem. Lett. 2023, 14, 10158−10165

calculations, imaginary part of the dielectric function with light polarization along the three lattice vectors, absorption coefficient of $Sn_2SbX_2I_3$ (X = S or Se), and the convergence of a number of valence (NO) and conduction bands (NV) used in the electron−hole interaction kernel for BSE calculations (PDF)

Transparent Peer Review report available (PDF)

AUTHOR INFORMATION

Corresponding Authors

Manish Kumar − *Department of Physics, Indian Institute of Technology Delhi, New Delhi 110016, India;* Present Address: M.K.: Physics Department and IRIS Adlershof, Humboldt-Universität zu Berlin, Zum Großen Windkanal 2, 12489 Berlin, Germany; orcid.org/0000-0001-9878-8032; Email: manish.kumar@physik.hu-berlin.de

Saswata Bhattacharya − *Department of Physics, Indian Institute of Technology Delhi, New Delhi 110016, India;* orcid.org/0000-0002-4145-4899; Phone: +91-11-2659 1359; Email: saswata@physics.iitd.ac.in

Author

Sajjan Sheoran − *Department of Physics, Indian Institute of Technology Delhi, New Delhi 110016, India;* orcid.org/0000-0002-6816-3944

Complete contact information is available at: https://pubs.acs.org/10.1021/acs.jpclett.3c02475

Notes

The authors declare no competing financial interest.

ACKNOWLEDGMENTS

M.K. acknowledges CSIR, India, for the senior research fellowship [Grant 09/086(1292)/2017-EMR-I]. S.S. acknowledges CSIR, India, for the senior research fellowship [Grant 09/086(1432)/2019-EMR-I]. S.B. acknowledges the financial support from SERB under a core research grant (Grant CRG/2019/000647). The authors acknowledge the High Performance Computing (HPC) facility at IIT Delhi for computational resources.

REFERENCES

(1) Hoye, R. L. Z.; Hidalgo, J.; Jagt, R. A.; Correa-Baena, J.-P.; Fix, T.; MacManus-Driscoll, J. L. The role of dimensionality on the optoelectronic properties of oxide and halide perovskites, and their halide derivatives. *Adv. Energy Mater.* **2022**, *12*, No. 2100499.

(2) Kojima, A.; Teshima, K.; Shirai, Y.; Miyasaka, T. Organometal halide perovskites as visible-light sensitizers for photovoltaic cells. *J. Am. Chem. Soc.* **2009**, *131*, 6050−6051.

(3) National renewable energy laboratory (NREL) best research-cell efficiency chart (accessed 2023-04-12).

(4) Ganose, A. M.; Savory, C. N.; Scanlon, D. O. Beyond methylammonium lead iodide: Prospects for the emergent field of ns^2 containing solar absorbers. *Chem. Commun.* **2017**, *53*, 20−44.

(5) Yoo, J. J.; Shin, S. S.; Seo, J. Toward efficient perovskite solar cells: Progress, strategies, and perspectives. *ACS Energy Lett.* **2022**, *7*, 2084−2091.

(6) Buchanan, M. Perovskite fever. *Nat. Phys.* **2020**, *16*, 996−996.

(7) Chen, Y.; Liu, X.; Wang, T.; Zhao, Y. Highly stable inorganic lead halide perovskite toward efficient photovoltaics. *Acc. Chem. Res.* **2021**, *54*, 3452−3461.

(8) Huang, Y.-T.; Kavanagh, S. R.; Scanlon, D. O.; Walsh, A.; Hoye, R. L. Z. Perovskite-inspired materials for photovoltaics and beyondfrom design to devices. *Nanotechnology* **2021**, *32*, No. 132004.

(9) Fabini, D. H.; Seshadri, R.; Kanatzidis, M. G. The underappreciated lone pair in halide perovskites underpins their unusual properties. *MRS Bull.* **2020**, *45*, 467−477.

(10) Ming, W.; Shi, H.; Du, M.-H. Large dielectric constant, high acceptor density, and deep electron traps in perovskite solar cell material $CsGeI_3$. *J. Mater. Chem. A* **2016**, *4*, 13852−13858.

(11) Kavanagh, S. R.; Savory, C. N.; Scanlon, D. O.; Walsh, A. Hidden spontaneous polarisation in the chalcohalide photovoltaic absorber $Sn_2SbS_2I_3$. *Mater. Horiz.* **2021**, *8*, 2709−2716.

(12) Nie, R.; Hu, M.; Risqi, A. M.; Li, Z.; Seok, S. I. Efficient and stable antimony selenoiodide solar cells. *Adv. Sci.* **2021**, *8*, No. 2003172.

(13) Nie, R.; Lee, K. S.; Hu, M.; Paik, M. J.; Seok, S. I. Heteroleptic tin-antimony sulfoiodide for stable and lead-free solar cells. *Matter* **2020**, *3*, 1701−1713.

(14) Nicolson, A.; Breternitz, J.; Kavanagh, S. R.; Tomm, Y.; Morita, K.; Squires, A. G.; Tovar, M.; Walsh, A.; Schorr, S.; Scanlon, D. O. Interplay of static and dynamic disorder in the mixed-metal chalcohalide $Sn_2SbS_2I_3$. *J. Am. Chem. Soc.* **2023**, *145*, 12509−12517.

(15) Olivier-Fourcade, J.; Jumas, J. C.; Maurin, M.; Philippot, E. Mise en évidence d'un nouveau sulfoiodure d'étain et d'antimoine $Sn_2SbS_2I_3$: Étude structurale. *Z. anorg. allg. Chem.* **1980**, *468*, 91−98.

(16) Ibanez, A.; Jumas, J.-C.; Olivier-Fourcade, J.; Philippot, E. Mise en évidence d'un désordre statistique dans les structures chalcogénoiodures d'étain et d'antimoine. *J. Solid State Chem.* **1984**, *55*, 83−91.

(17) Palazon, F. Metal chalcohalides: Next generation photovoltaic materials? *Sol. RRL* **2022**, *6*, No. 2100829.

(18) Choi, Y. C.; Nie, R. Heavy pnictogen chalcohalides for efficient, stable, and environmentally friendly solar cell applications. *Nanotechnology* **2023**, *34*, No. 142001.

(19) Zheng, F.; Tan, L. Z.; Liu, S.; Rappe, A. M. Rashba spin-orbit coupling enhanced carrier lifetime in $CH_3NH_3PbI_3$. *Nano Lett.* **2015**, *15*, 7794−7800.

(20) Etienne, T.; Mosconi, E.; De Angelis, F. Dynamical origin of the Rashba effect in organohalide lead perovskites: A key to suppressed carrier recombination in perovskite solar cells? *J. Phys. Chem. Lett.* **2016**, *7*, 1638−1645.

(21) Zhang, X.; Shen, J.-X.; Van de Walle, C. G. Three-dimensional spin texture in hybrid perovskites and its impact on optical transitions. *J. Phys. Chem. Lett.* **2018**, *9*, 2903−2908.

(22) Chakraborty, S.; Nazeeruddin, M. K. The status quo of Rashba phenomena in organic-inorganic hybrid perovskites. *J. Phys. Chem. Lett.* **2021**, *12*, 361−367.

(23) Yamada, Y.; Kanemitsu, Y. Electron-phonon interactions in halide perovskites. *NPG Asia Mater.* **2022**, *14*, 48.

(24) Hohenberg, P.; Kohn, W. Inhomogeneous electron gas. *Phys. Rev.* **1964**, *136*, B864−B871.

(25) Kohn, W.; Sham, L. J. Self-consistent equations including exchange and correlation effects. *Phys. Rev.* **1965**, *140*, A1133−A1138.

(26) Hedin, L. New method for calculating the one-particle Green's function with application to the electron-gas problem. *Phys. Rev.* **1965**, *139*, A796−A823.

(27) Hybertsen, M. S.; Louie, S. G. First-principles theory of quasiparticles: Calculation of band gaps in semiconductors and insulators. *Phys. Rev. Lett.* **1985**, *55*, 1418−1421.

(28) Albrecht, S.; Reining, L.; Del Sole, R.; Onida, G. *Ab initio* calculation of excitonic effects in the optical spectra of semiconductors. *Phys. Rev. Lett.* **1998**, *80*, 4510−4513.

(29) Rohlfing, M.; Louie, S. G. Electron-hole excitations in semiconductors and insulators. *Phys. Rev. Lett.* **1998**, *81*, 2312−2315.

(30) Sendner, M.; Nayak, P. K.; Egger, D. A.; Beck, S.; Müller, C.; Epding, B.; Kowalsky, W.; Kronik, L.; Snaith, H. J.; Pucci, A.; et al. Optical phonons in methylammonium lead halide perovskites and implications for charge transport. *Mater. Horiz.* **2016**, *3*, 613−620.

(31) Frost, J. M. Calculating polaron mobility in halide perovskites. *Phys. Rev. B* **2017**, *96*, No. 195202.

(32) Zhao, X.-G.; Dalpian, G. M.; Wang, Z.; Zunger, A. Polymorphous nature of cubic halide perovskites. *Phys. Rev. B* **2020**, *101*, No. 155137.
(33) Octavio de Araujo, L.; Rêgo, C. R. C.; Wenzel, W.; Sabino, F. P.; Guedes-Sobrinho, D. Impact of the polymorphism and relativistic effects on the electronic properties of inorganic metal halide perovskites. *J. Phys. Chem. C* **2022**, *126*, 2131−2140.
(34) Jain, A.; Ong, S. P.; Hautier, G.; Chen, W.; Richards, W. D.; Dacek, S.; Cholia, S.; Gunter, D.; Skinner, D.; Ceder, G.; et al. Commentary: The Materials Project: A materials genome approach to accelerating materials innovation. *APL Mater.* **2013**, *1*, No. 011002.
(35) Klimeš, J. c. v.; Bowler, D. R.; Michaelides, A. Van der Waals density functionals applied to solids. *Phys. Rev. B* **2011**, *83*, No. 195131.
(36) Starosta, V. I.; Kroutil, J.; Beneš, L. Preparation and fundamental physical properties of $Sn_2SbS_2I_3$ and $Pb_2SbS_2I_3$ compounds. *Cryst. Res. Technol.* **1990**, *25*, 1439−1442.
(37) Ramazashvili, R. Kramers degeneracy in a magnetic field and Zeeman spin-orbit coupling in antiferromagnetic conductors. *Phys. Rev. B* **2009**, *79*, No. 184432.
(38) Autieri, C.; Barone, P.; Sławińska, J.; Picozzi, S. Persistent spin helix in Rashba-Dresselhaus ferroelectric $CsBiNb_2O_7$. *Phys. Rev. Materials* **2019**, *3*, No. 084416.
(39) Sheoran, S.; Bhumla, P.; Bhattacharya, S. Emergence of cubic ordered full-plane persistent spin textures in lead-free materials. *Phys. Rev. Materials* **2022**, *6*, No. 094602.
(40) Sheoran, S.; Kumar, M.; Bhumla, P.; Bhattacharya, S. Rashba spin splitting and anomalous spin textures in the bulk ferroelectric oxide perovskite KIO_3. *Mater. Adv.* **2022**, *3*, 4170−4178.
(41) Aroyo, M. I.; Perez-Mato, J. M.; Capillas, C.; Kroumova, E.; Ivantchev, S.; Madariaga, G.; Kirov, A.; Wondratschek, H. Bilbao Crystallographic Server: I. Databases and crystallographic computing programs. *Z. Kristallogr. Cryst. Mater.* **2006**, *221*, 15−27.
(42) Dresselhaus, M. S.; Dresselhaus, G.; Jorio, A. *Group theory: Application to the physics of condensed matter*; Springer: Berlin, 2008.
(43) Zhao, H. J.; Nakamura, H.; Arras, R.; Paillard, C.; Chen, P.; Gosteau, J.; Li, X.; Yang, Y.; Bellaiche, L. Purely cubic spin splittings with persistent spin textures. *Phys. Rev. Lett.* **2020**, *125*, No. 216405.
(44) Moriya, R.; Sawano, K.; Hoshi, Y.; Masubuchi, S.; Shiraki, Y.; Wild, A.; Neumann, C.; Abstreiter, G.; Bougeard, D.; Koga, T.; et al. Cubic Rashba spin-orbit interaction of a two-dimensional hole gas in a strained-Ge/SiGe quantum well. *Phys. Rev. Lett.* **2014**, *113*, No. 086601.
(45) Xiong, J.-X.; Guan, S.; Luo, J.-W.; Li, S.-S. Orientation-dependent Rashba spin-orbit coupling of two-dimensional hole gases in semiconductor quantum wells: Linear or cubic. *Phys. Rev. B* **2022**, *105*, No. 115303.
(46) Bernevig, B. A.; Orenstein, J.; Zhang, S.-C. Exact SU(2) symmetry and persistent spin helix in a spin-orbit coupled system. *Phys. Rev. Lett.* **2006**, *97*, No. 236601.
(47) Sheoran, S.; Monga, S.; Phutela, A.; Bhattacharya, S. Coupled spin-valley, Rashba effect, and hidden spin polarization in WSi_2N_4 family. *J. Phys.Chem. Lett.* **2023**, *14*, 1494−1503.
(48) Baranowski, M.; Plochocka, P. Excitons in metal-halide perovskites. *Adv. Energy Mater.* **2020**, *10*, No. 1903659.
(49) Kumar, M.; Singh, A.; Gill, D.; Bhattacharya, S. Optoelectronic properties of chalcogenide perovskites by many-body perturbation theory. *J. Phys. Chem. Lett.* **2021**, *12*, 5301−5307.
(50) Ōsaka, Y. Theory of polaron mobility. *Prog. Theor. Phys.* **1961**, *25*, 517−536.
(51) Feynman, R. P. Slow electrons in a polar crystal. *Phys. Rev.* **1955**, *97*, 660.
(52) Ōsaka, Y. Polaron state at a finite temperature. *Prog. Theor. Phys.* **1959**, *22*, 437−446.
(53) Miyata, K.; Meggiolaro, D.; Trinh, M. T.; Joshi, P. P.; Mosconi, E.; Jones, S. C.; De Angelis, F.; Zhu, X.-Y. Large polarons in lead halide perovskites. *Sci. Adv.* **2017**, *3*, No. e1701217.
(54) Hellwarth, R. W.; Biaggio, I. Mobility of an electron in a multimode polar lattice. *Phys. Rev. B* **1999**, *60*, 299.
(55) Basera, P.; Singh, A.; Gill, D.; Bhattacharya, S. Capturing excitonic and polaronic effects in lead iodide perovskites using many-body perturbation theory. *J. Mater. Chem. C* **2021**, *9*, 17113−17123.
(56) Jain, M.; Gill, D.; Bhumla, P.; Basera, P.; Bhattacharya, S. Theoretical insights to excitonic effect in lead bromide perovskites. *Appl. Phys. Lett.* **2021**, *118*, No. 192103.
(57) Basera, P.; Bhattacharya, S. Chalcogenide perovskites (ABS_3; A = Ba, Ca, Sr; B = Hf, Sn): An emerging class of semiconductors for optoelectronics. *J. Phys. Chem. Lett.* **2022**, *13*, 6439−6446.
(58) Kresse, G.; Furthmüller, J. Efficiency of ab-initio total energy calculations for metals and semiconductors using a plane-wave basis set. *Comput. Mater. Sci.* **1996**, *6*, 15−50.
(59) Kresse, G.; Joubert, D. From ultrasoft pseudopotentials to the projector augmented-wave method. *Phys. Rev. B* **1999**, *59*, 1758−1775.
(60) Blöchl, P. E. Projector augmented-wave method. *Phys. Rev. B* **1994**, *50*, 17953−17979.
(61) Monkhorst, H. J.; Pack, J. D. Special points for Brillouin-zone integrations. *Phys. Rev. B* **1976**, *13*, 5188−5192.
(62) Ganose, A. M.; Jackson, A. J.; Scanlon, D. O. sumo: Command-line tools for plotting and analysis of periodic ab initio calculations. *Journal of Open Source Software* **2018**, *3*, 717.
(63) Tkatchenko, A.; Scheffler, M. Accurate molecular van der Waals interactions from ground-state electron density and free-atom reference data. *Phys. Rev. Lett.* **2009**, *102*, No. 073005.

https://doi.org/10.1021/acs.jpclett.3c02475
J. Phys. Chem. Lett. 2023, 14, 10158−10165